

Current enhancement via a TiO₂ window layer for CSS Sb₂Se₃ solar cells: performance limits and high V_{oc}

Laurie J. Phillips, Christopher N. Savory, Oliver S. Hutter, Peter J. Yates, Huw Shiel, Silvia Mariotti, Leon Bowen, Max Birkett, Ken Durose, David O. Scanlon, and Jonathan D. Major

Abstract— Antimony selenide (Sb₂Se₃) is an emerging chalcogenide photovoltaic absorber material that has been the subject of increasing interest in recent years; demonstrating rapid efficiency increases with a material that is simple, abundant, and stable. This work examines the material from both a theoretical and practical standpoint. The theoretical viability of Sb₂Se₃ as a solar photovoltaic material is assessed and the maximum spectroscopically limited performance is estimated, with a 200 nm film expected to be capable of achieving a photon conversion efficiency of up to 28.2%. By adapting an existing CdTe close-spaced sublimation (CSS) process, Sb₂Se₃ material with large rhubarb-like grains is produced and solar cells are fabricated. We show the established CdS window layer is unsuitable for use with CSS, due to intermixing during higher temperature processing. Substituting CdS with the more stable TiO₂, a power conversion efficiency (PCE) of 5.5% and an open circuit voltage (V_{oc}) of 0.45 V are achieved; the voltage exceeding current champion devices. This work demonstrates the potential of CSS for scalable Sb₂Se₃ deposition and highlights the promise of Sb₂Se₃ as an abundant and low-toxicity material for solar applications.

Index Terms— Antimony selenide, Sb₂Se₃, CSS, TiO₂, titania, CdS, SLME.

I. INTRODUCTION

DIVERSIFICATION of the viable base of photovoltaic (PV) solar cell technologies remains of primary interest to the field. Silicon is still dominant, but thin film technologies with superior optical and material properties have begun to establish themselves as alternatives [1], [2]. Antimony selenide [3] (Sb₂Se₃) is an emerging material that meets a number of

desirable criteria; being a single phase, stable V-VI binary chalcogenide material [4], with a near-ideal band-gap of 1.1-1.3 eV and a high absorption coefficient ($\sim 10^5$ cm⁻¹) [5], [6]. Interestingly, the crystal is composed of one-dimensional, covalently-bonded (Sb₄Se₆)_n ribbons parallel to the c-axis (*Pbnm* space group) [7], held together by van der Waals forces as in Fig. 1(a) [8]. The consequential reduction in grain boundary dangling-bond density mitigates non-radiative recombination losses, often a limiting factor in polycrystalline photovoltaic materials [9]. Furthermore, it has been suggested by Brandt *et al.* [10] that many of the desirable properties of hybrid perovskites (i.e. high minority carrier lifetimes) may in part derive from containing 6s² electron pairs on the cation. Therefore, other materials which have an ns² electron configuration, such as Sb₂Se₃, with its partially oxidized post-transition metal Sb³⁺, should be explored [11]. Although the material itself had previously been studied, research into Sb₂Se₃ photovoltaic devices has only progressed recently, with the first report of a notable efficiency being 3.21% by Choi *et al.* in 2014 [12]. Since then, despite the comparative paucity of cell work, <100 papers [13], progress has been rapid, reaching 5.6% for a CdS/Sb₂Se₃ heterojunction in 2016 [3] and more recently 5.9% for a ZnO/Sb₂Se₃ heterojunction [4], and the current record; 7.6% for CdS/Sb₂Se₃ [14]. Despite its short development time, Sb₂Se₃ has already surpassed the efficiencies of long-investigated binary inorganics such as SnS and FeS₂. Given the nascent nature of the research field, and the limited understanding of the device structures and defect composition, there is a tremendous amount of potential for further development of this emerging PV material.

[†]This paragraph of the first footnote will contain the date on which you submitted your paper for review. This work was supported by EPSRC grants EP/N014057/1, EP/P02484X/1 (SUPERGEN), EP/M014797/1, and EP/N015800/1. Computational work in this article was performed on the ARCHER U.K. National Supercomputing Service (<http://www.archer.ac.uk>), via our membership of the U.K.'s HEC Materials Chemistry Consortium, which is funded by EPSRC (Grant No. EP/ L000202), and the UCL Legion (Legion@UCL) and Grace (Grace@UCL) HPC Facilities. D.O.S. acknowledges funding through EPSRC (Grant No. EP/N01572X/1) and membership of the Materials Design Network. C.N.S. is grateful to EPSRC and the Department of Chemistry at UCL for the provision of a Doctoral Training Partnership studentship (ref No. 1492829). We thank Mark A. Farnworth for TOF-SIMS analysis and Tim Veal for helpful discussions when preparing this manuscript.

L. J. Phillips, O. S. Hutter, P. J. Yates, H. Shiel, S. Mariotti, M. Birkett, K. Durose, and J. D. Major are with the Stephenson Institute for Renewable Energy, University of Liverpool, UK (e-mail: Laurie.Phillips@liverpool.ac.uk,

O.S.Hutter@liverpool.ac.uk, P.J.Yates@liverpool.ac.uk, sghshiel@liverpool.ac.uk, Silvia.Mariotti@liverpool.ac.uk, M.Birkett@liverpool.ac.uk, Ken.Durose@liverpool.ac.uk, Jon.Major@liverpool.ac.uk).

C. N. Savory is with the University College London, Kathleen Lonsdale Building, Department of Chemistry, 20 Gordon Street, London WC1H 0AJ, UK, and the Thomas Young Centre, University College London, Gower Street, London WC1E 6BT, UK (e-mail: christopher.savory.14@ucl.ac.uk)

L. Bowen, is with the G. J. Russell Microscopy Facility, University of Durham, Durham, UK (e-mail: leon.bowen@durham.ac.uk)

D. O. Scanlon is with the University College London, Kathleen Lonsdale Building, Department of Chemistry, 20 Gordon Street, London WC1H 0AJ, UK, the Thomas Young Centre, University College London, Gower Street, London WC1E 6BT, UK, and the Diamond Light Source Ltd., Diamond House, Harwell Science and Innovation Campus, Didcot, Oxfordshire OX11 0DE, UK (e-mail: d.scanlon@ucl.ac.uk)

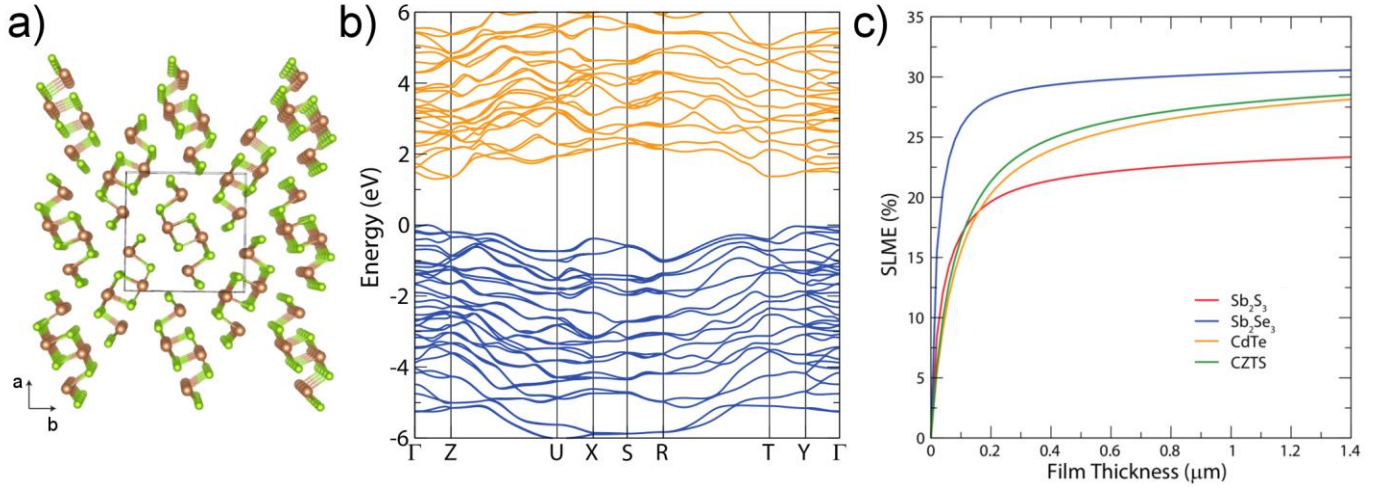


Fig. 1. Theoretical calculations of the properties of Sb_2Se_3 (a) Structure of Sb_2Se_3 viewed down the [001] axis. (b) Electronic band structure of Sb_2Se_3 . The valence band is in blue, with the conduction band in orange. The valence band maximum is normalized to $E=0$. K-points of notable symmetry in the P-orthorhombic Brillouin Zone are defined with $\Gamma = (0, 0, 0)$, $Z = (0.5, 0, 0)$, $U = (0.5, 0, 0.5)$, $X = (0, 0, 0.5)$, $S = (0, -0.5, 0.5)$, $R = (0.5, -0.5, 0.5)$, $T = (0.5, -0.5, 0)$ and $Y = (0, -0.5, 0)$ [51]. (c) Plot of spectroscopic limited maximum efficiency (SLME) against film thickness, for Sb_2Se_3 and other champion solar absorbers.

Sb_2Se_3 solar cells have been successfully fabricated using thermal evaporation [15], sputtering [16], electro-deposition [17], spin-coating [12], and close-spaced sublimation (CSS) [6], [18]–[20], and in superstrate and substrate configuration [21]–[23]. The scalability of CSS, its propensity for large grained material, and rapidity of deposition [24], are crucial to the commercial success of CdTe solar cells. Given the similarity in the previously reported device structures between the two technologies $\text{SnO}_2\text{:F/CdS/CdTe}$ and $\text{SnO}_2\text{:F/CdS/Sb}_2\text{Se}_3$, transfer of the premier CdTe deposition technique was a logical progression. Previous work by Zhou *et al.* [3] used a rapid thermal evaporation (RTE) deposition technique similar to CSS. However, their process is performed under vacuum, whereas one of the key characteristics of CSS deposition is the use of an inert [25], or reactive gas ambient [26]. This modification is key, and the reason that films deposited by Zhou *et al.* [3] have the smaller grain size characteristic of thermally evaporated material. In this work, we demonstrate that CSS, a proven industrially scalable process, is highly suited for Sb_2Se_3 deposition. We show that CSS produces material with a very different structure to other techniques resulting in exceptionally large grains, but that its use precludes the use of a CdS partner layer. However, due to the different material quality produced by CSS a $\text{TiO}_2/\text{Sb}_2\text{Se}_3$ heterojunction is shown to be effective. It can produce devices with efficiencies of 5.5%, comparable to the highest reported for devices with TiO_2 [23], and having V_{oc} values exceeding recent record devices with any partner layer [14], [27].

II. EXPERIMENTAL DETAILS

Calculations were performed using Density Functional Theory (DFT) within periodic boundary conditions using the Vienna *Ab Initio* Simulation Package (VASP) [28]–[31]. The screened hybrid exchange correlation functional HSE06 was used [32], for electronic structure and optical calculations, and geometry optimization of both bulk and defect supercells of Sb_2Se_3 . Due to the layered nature of the Sb_2Se_3 structure, the D3 dispersion

correction from Grimme *et al.* was also included in all calculations [33], while spin-orbit coupling (SOC) was included for all bulk electronic calculations. For the comparative optical study with CdTe and $\text{Cu}_2\text{ZnSnS}_4$ (CZTS), HSE06 alone was used for all calculations. HSE06 includes 75% exchange and full correlation from the Generalized Gradient Approximation (GGA) functional PBE [34], and 25% exchange from Hartree-Fock, which is range-screened using a parameter of $\omega = 0.11 \text{a}_0^{-1}$. Scalar relativistic pseudopotentials were used, with the projector-augmented wave method used to describe valence-core electron interaction, which allows accuracy on par with all-electron methods [35]. Optical properties were obtained using the method of Furthmüller *et al.* to obtain the high frequency dielectric function, while the ionic contribution to the dielectric function was calculated with Density Functional Perturbation Theory (DFPT) at the PBEsol level [36]. A plane wave energy cut-off 350 eV was used for all calculations, with a Γ -centered k-point mesh of $2 \times 6 \times 2$ used for bulk calculations of Sb_2Se_3 , which was doubled for optical calculations (k-point meshes of equivalent density were used for optical calculations of CZTS and CdTe). These values were obtained through convergence testing on the total energy, using criteria of 1 meV per atom and 10 meV per atom for k-mesh and energy cut-off respectively. Spectroscopic limited maximum efficiency (SLME) utilizes an absorption spectrum $a(E) = 1 - e^{-2\alpha(E)L}$, where $\alpha(E)$ is the *ab initio* calculated absorption coefficient and L the film thickness, in place of the stepwise function used by Shockley and Queisser. It also includes the fraction of current from radiative electron-hole recombination as $f_r = e^{-\Delta/k_B T}$ (k_B is the Boltzmann constant, T the temperature, and Δ is the difference between the lowest direct allowed transition and the fundamental band gap, E_g) reflecting the greater influence of non-radiative recombination on highly indirect gap materials [37].

The evaporated Sb_2Se_3 layers for characterization were deposited using a Moorfields™ multi-source evaporation chamber with a separation distance of 20 cm between source and substrate. The substrate was heated to a range of

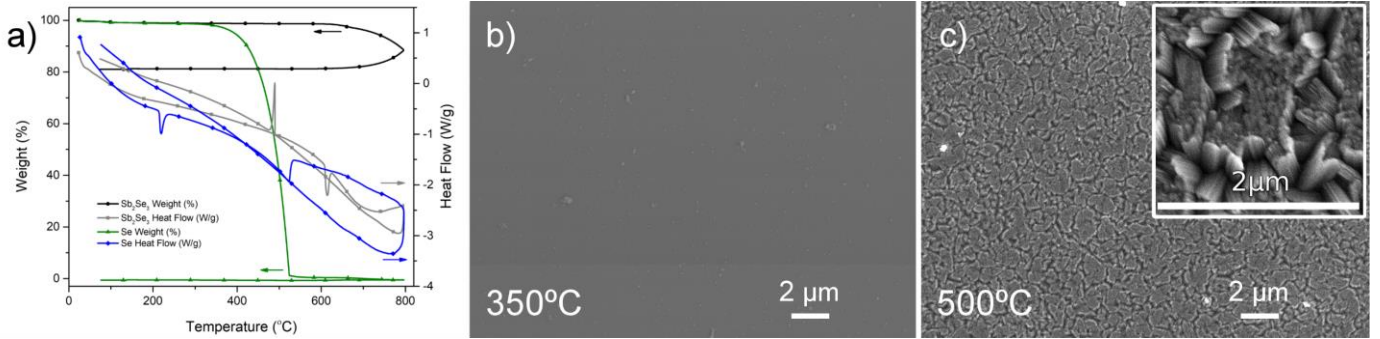


Fig. 2. The properties of evaporated Sb_2Se_3 . a) Differential Scanning Calorimetry of Sb_2Se_3 and Se. Taken using a ramp rate of $5^\circ\text{C}/\text{min}$, showing the relative stability of Sb_2Se_3 compared to Se in the working experimental range ($400 - 475^\circ\text{C}$). b) and c) SEM images of evaporated Sb_2Se_3 layers deposited with substrate temperatures of 350°C and 500°C respectively. The inset is a $2 \times 2 \mu\text{m}$ magnification of the 500°C sample. Evaporated Sb_2Se_3 shows no grain structure until ca. 450°C . However, unlike the CSS material, the grains at these temperatures are very small, with the apparent larger grains in the 500°C sample consisting of agglomerations of distinct smaller sub-grains.

temperatures between room temperature (RT) and 500°C , and rotated during deposition. This material had no post-growth treatment or annealing. CSS growth of Sb_2Se_3 was conducted in a custom-built close space sublimation apparatus with controlled variable pressure built by Electro-Gas Systems Ltd. CSS material was carried out by first evacuating the system while the source was heated to 350°C via an infra-red heater. 10 Torr of N_2 was then introduced into the chamber and the temperature increased to 475°C . Deposition time began when the temperature reached 475°C and continued for 15 mins after which the pressure was abruptly increased to 300 Torr to halt deposition and the heater was switched off. The substrate was not intentionally heated during the deposition, but due to being very close to the source, reached ca. 425°C . The substrate was positioned ~ 5 mm above the source tray and material travelled down the temperature gradient between the source and substrate, condensing on the marginally cooler substrate positioned above.

Devices were fabricated using TEC10 (FTO) coated glass from NSG Ltd., coated with two different window layers; CdS and TiO_2 . A ZnO buffer layer was also used for the CdS window to enable a thinner CdS layer. The ZnO layer was sputtered at 150W for 50 minutes at RT. The CdS was then sputtered on top without breaking vacuum at 60W for 15 minutes, with the substrate heated to 200°C . The TiO_2 window layer was fabricated using spin-coating. Two solutions of titanium-isopropoxide in ethanol were made up at concentrations of 0.15 M and 0.3 M with stirring at room temperature. These were spun sequentially onto the TEC10 substrate at 3000 rpm, with each layer dried at 120°C for 10 mins. The completed substrate was then sintered at 450°C for 30 mins in air. The Sb_2Se_3 absorber was deposited in the same way as described for the characterization layers. The devices were completed by evaporating 0.25 cm^2 gold contacts through a shadow mask. SEM measurements were taken using a JEOL 7001F and the (S)TEM measurements used a JEOL 2100F. EQE measurements were taken with a Bentham PVE300, Illuminated J - V curves were taken using a TS Space Systems Class A "AAA100" solar simulator operating at AM1.5 conditions (calibrated using a certified PV Measurements GaAs cell), current and voltage measurements taken with a Keithley

TABLE I
DIELECTRIC CONSTANTS FOR Sb_2Se_3 .

	Q_{xx}	Q_{yy}	Q_{zz}	Q_{AV}
High frequency	13.67	18.68	19.35	17.23
Lattice response	3.46	55.61	68.17	42.41
Total response	17.13	74.29	87.52	59.65

Calculated using DFT, given along cell directions and as an isotropic average (Q_{AV}).

2400 scanning from -1 V to 1 V in 20 mV steps at a rate of 271 mV/s. C - V measurements were taken with a Solartron 1260A impedance analyzer with a 1296A dielectric interface. J - V and C - V measurements were all performed in air at room temperature, without preconditioning. Differential Scanning Calorimetry (DSC) was carried out using a TA instruments SDT Q600 with an argon purge gas, alumina crucibles with lids, and a heating rate of $5^\circ\text{C}/\text{min}$. TOF-SIMS was performed using an ION-TOF TOF-SIMS V instrument using 25 KeV Bi^{3+} as the analysis beam and 1 KeV Cs^+ as the sputtering beam.

III. RESULTS

A. Evaluation of Sb_2Se_3 as a photovoltaic material

The optical properties of Sb_2Se_3 are crucial to its potential as a photovoltaic absorber. The electronic band structure of Sb_2Se_3 , calculated with HSE06+D3+SOC, is shown in Fig. 1(b). The indirect fundamental band gap is 1.299 eV, which is consistent with both low temperature photo-reflectance and previous quasiparticle GW calculations [6], [38]. The direct band-gap is only 0.025 eV higher at 1.324 eV meaning Sb_2Se_3 can be characterized as a near-direct bandgap material. The theoretical absorption coefficient, was found to be $>1 \times 10^4 \text{ cm}^{-1}$ for energies above 1.5 eV, increasing to $1 \times 10^5 \text{ cm}^{-1}$ at 1.8 eV, indicating a sharp and strong absorption edge. The high frequency response and the static response, calculated using Density Functional Perturbation Theory (DFPT), are given in Table 1, separated into the individual diagonal contributions to the overall tensor. For both high frequency and static responses, the response is weakest along x , the direction broadly corresponding to the 'thin' face of the 1D ribbon, but while the

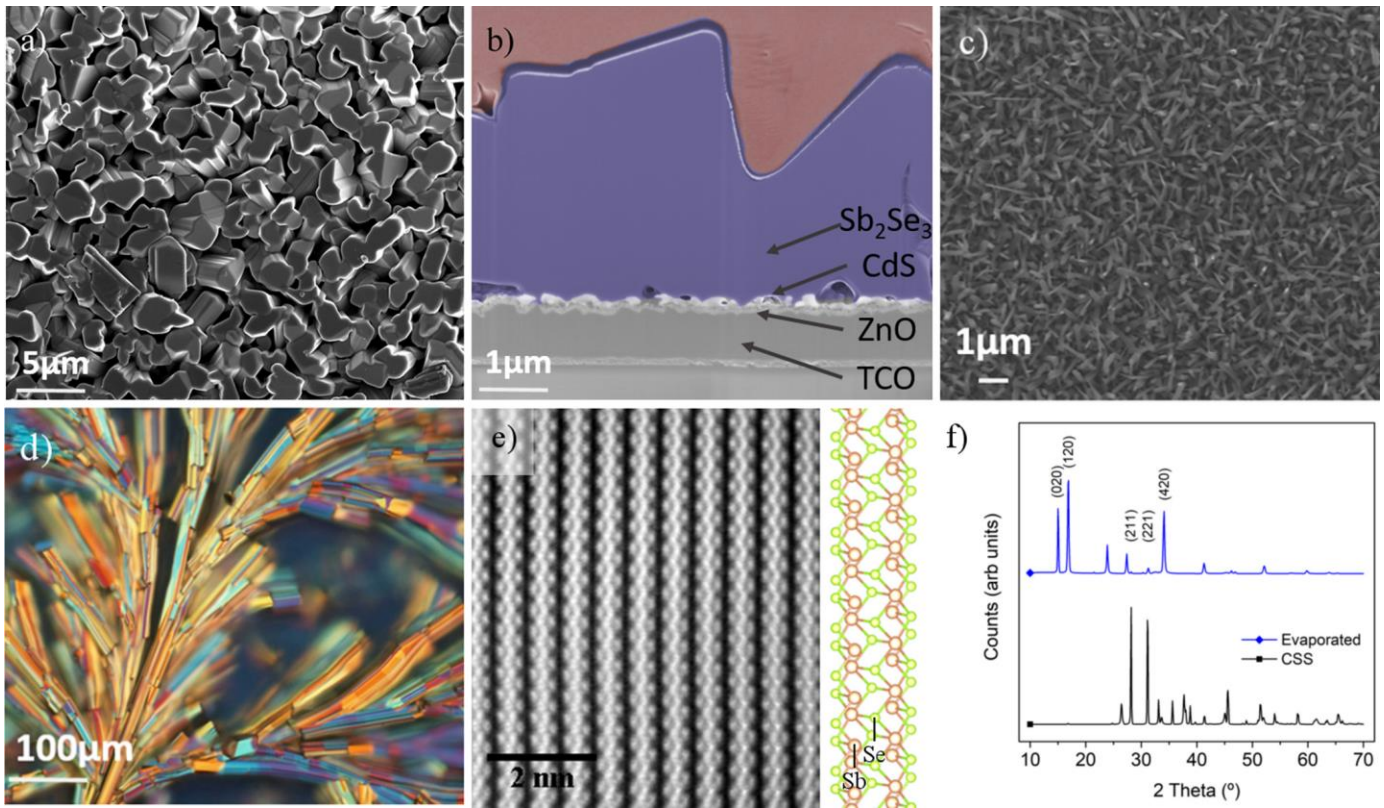


Fig. 3. The structure of Sb_2Se_3 grown by CSS and evaporation at various conditions. a) SEM image of the surface of Sb_2Se_3 showing the large grains produced by CSS grown at T_{source} of 475°C and pressure of 10 Torr N_2 . b) SEM cross-section of CSS deposited Sb_2Se_3 on CdS, showing the continuous grains spanning the entire layer (growth conditions as 2a). c) Nanowire formation for a CSS deposition at a lower T_{source} of 400°C and 10 Torr of N_2 . d) Optical microscope image of large crystals of Sb_2Se_3 grown at a high pressure of 200 Torr of N_2 . e) HRTEM of evaporated Sb_2Se_3 showing $(\text{Sb}_4\text{Se}_6)_n$ nanoribbons projected onto the $Pbnm$ (120) plane with crystal schematic inset. f) XRD of evaporated and CSS deposited Sb_2Se_3 highlighting the reflections at 15.0° , 16.8° , 28.1° , 31.1° , and 34.4° corresponding to $Pbnm$ planes (020), (120), (211), (221) and (420) respectively.

high frequency response is relatively isotropic, the lattice response is an order of magnitude stronger along y and z . The strength of the combined dielectric constant in these two directions is above that for methylammonium lead iodide, and is notable, considering that high dielectric constants have been highlighted as a potentially crucial property in defect tolerant semiconductors due to screening charge carriers from defects [10], [11], [39]. Combining the theoretical optical absorption with the band gap allows the calculation of the SLME, a screening metric for thin film photovoltaics [37]. SLME was calculated as a function of film thickness for both Sb_2Se_3 and Sb_2S_3 , as well as the direct-gap absorbers CdTe and $\text{Cu}_2\text{ZnSnS}_4$ (CZTS) for comparison in Fig. 1(c). SLME assumes a perfect bulk system, but it appears that Sb_2Se_3 is not disadvantaged by its indirect gap, with its SLME being 28.2% for a film thickness of 200 nm, far outperforming CdTe and CZTS with 20.3% and 21.5% respectively.

B. Microstructure of Sb_2Se_3 deposited via CSS

Many selenides, including Sb_2Se_3 , undergo partial dissolution by decomposition when they sublime [40]. These endothermic reactions produce volatile selenium-poor moieties, in addition to selenium. However, analysis using differential scanning calorimetry (DSC), shown in Fig. 2(a), reveals that Sb_2Se_3 remains stable until above 600°C . In this work, the Sb_2Se_3

deposition was carried out at $<500^\circ\text{C}$ via CSS, therefore we do not expect the Sb_2Se_3 to lose selenium and become non-stoichiometric during deposition. The DSC also shows that any excess selenium in the source material should be lost at 400°C , so the source will become more stoichiometric during preconditioning and repeated use. For comparison, the sulfur analogue, Sb_2S_3 , undergoes decomposition with sulfur loss at around 250°C , a much lower temperature than for Sb_2Se_3 , meaning it will require post-growth sulfurization and is therefore less suitable for CSS deposition.

Thermally evaporated Sb_2Se_3 films were deposited with substrate temperatures from room temperature to 500°C , with 350°C and 500°C , shown in scanning electron microscope (SEM) images Fig. 2(b) and 2(c). Only a small amount of grain structure is visible, and only then at temperatures higher than *ca.* 450°C , with small sub-domains clear from the inset in Fig. 2(c). In contrast, Fig. 3(a) shows an SEM image of the back surface for a Sb_2Se_3 film deposited using CSS at 450°C under a nitrogen pressure of 10 Torr. A focused ion beam (FIB) milled cross section of the same device, showing the $\text{SnO}_2/\text{F}/\text{ZnO}/\text{CdS}/\text{Sb}_2\text{Se}_3$ layers, is depicted in Fig. 3(b). From these images, it is clear that CSS growth produces significantly larger grains with distinctively columnar, rhubarb-like, individual domains larger than $1\ \mu\text{m}$. This is significant as the layer itself is of a similar order of thickness ($\sim 3\ \mu\text{m}$) and

therefore it is very likely that most grains span the entire layer, thus presenting no lateral barriers to charge extraction and minimizing potential recombination sites. The FIB cross-section of the layer shown in Fig. 3(b) provides further evidence for this as the layer has no visible grain boundaries between the CdS and the platinum coating on the top surface. It is possible to further increase the grain size using higher temperatures or increased nitrogen pressure [41], but this can induce the formation of pinholes which cause deleterious shunting at lower film thicknesses. However, while the top-down SEM appears to show grains separated by voids, the cross-section shows that some grains coalesce below the surface, as in Fig. 3(b), while in others the grain boundary is still visible. This suggests that the material is soft and relatively tolerant, presumably due to the lack of rigidity in the ribbons, leading to better coverage and correspondingly fewer shorting pathways. A reduced substrate deposition temperature of 400°C alters the growth of Sb₂Se₃ into self-catalyzed dense nanowire arrays, as shown in Fig. 3(c). These nanowire arrays are noticeably different, appearing blacker than films deposited at higher temperatures. Despite improved optical absorption, these nanowire arrays are unsuitable for device fabrication as their adhesion to the substrate is poor, being removed from the surface by the slightest contact. Due to this problem, these films were not used for devices. This is in stark contrast to device-quality films grown at 475°C in Fig. 3(a), where strong adhesion is observed. Increasing the pressure of the deposition also has a dramatic effect on the film with very large dendritic-like structures forming. Fig. 3(d) shows an optical image of a deposition with grains larger than 100 μm, which were formed by maintaining the same substrate temperature as for cell quality layers but setting the initial deposition pressure to 200 Torr for the first 10 seconds of growth. A high gas pressure allows conditions of high temperature but slow material flux favoring island growth [41]. While interesting, the large voids mean that this is unsuitable for PV applications. This highlights that careful selection of the growth conditions are required. The 1D nature of the material can be confirmed using high resolution TEM analysis. Fig. 3(e) is a TEM image of a Sb₂Se₃ film showing the distinct ribbon-like structure of the material, with a labelled atomistic diagram inset. The resultant micro-wire, rhubarb-like, appearance is therefore understandably different from the more typical grain structure of 3D lattice materials such as CdTe and does not follow the standard structure zone growth model [42].

Optimal photovoltaic performance and charge separation have been reported for crystal grains orientated with ribbon axes inclined from the substrate: due to improved conduction along the ribbon axes [3]. The XRD patterns in Fig. 3(f) reveal a key difference between films deposited at 450°C by CSS and typical thermal evaporation. Evaporated material has prominent reflections at 15.0° and 16.8° corresponding respectively to (020)- and (120)-orientated grains (*Pbnm* setting); the ribbons in such grains lie parallel to the substrate, giving poor orthogonal conductivity as excited carriers must hop between neighboring ribbons. Conversely, while CSS material has no significant reflections below 25°, major reflections are seen at 28.1° and 31.1° corresponding to the (211) and (221) planes respectively, indicating ribbons inclined at 37° and 44° relative to the substrate normal. Hence CSS-deposited grains are

quantifiably different and offer enhanced photovoltaic charge extraction. We note that it is possible to describe the crystal planes and axes using either the *Pbnm* or *Pnma* settings of space group 62, which are equivalent; rotating the *Pbnm* coordinate system (a,b,c) (and Miller indices) gives the *Pnma* (b,c,a) system [43]. For these results, we have used the *Pbnm* setting for which the covalently bonded ribbons lie along [001].

C. Device studies

Initial studies were made to fabricate Sb₂Se₃-based cells by simply replacing the CdTe absorber from our standard CdTe device stack to give a structure of FTO/ZnO/CdS/Sb₂Se₃/Au as shown in Fig. 4(a). This incorporates the typical high resistance transparent (HRT) oxide plus CdS buffer layer structure that allows thinner CdS to be utilized and minimizes performance loss [44]. It is worth noting here that the optimized Sb₂Se₃ film thickness for our devices (2-3 μm) is significantly greater than the <500 nm generally reported elsewhere. The best *J-V* curve from this cell architecture is shown in Fig. 4(b), with associated EQE, normalized EQE, and *C-V* curves in Fig. 4(c), 4d, and 4e respectively, and device performance parameters listed in Table 2. While the *V_{oc}* values compare favourably to the best in literature, the *J_{sc}* and fill factor are low for the CdS sample, compared to both TiO₂ and literature [14], [27]. This is partly explained by parasitic absorption, given the relatively small (2.42 eV) bandgap of CdS, but the EQE measurements also suggested the formation of an intermediate CdSe layer due to intermixing between CdS and Sb₂Se₃. CdS cells show low quantum efficiency in the region between the 1.18 and 1.74 eV band gaps of Sb₂Se₃ and CdSe (710 nm to 1050 nm) but improves at higher photon energies. Such out-diffusion from the CdS layer is a well-established phenomenon in CdTe solar cells and indeed is known to be more pronounced with CSS than with lower temperature growth methods [45]. Carrier extraction from photons below the CdSe bandgap, collected in the Sb₂Se₃ layer, is lower and implies a limiting conduction-band offset between Sb₂Se₃ and CdSe. As shown in Fig. 5(a,i), CdSe introduces a potential barrier, preventing charge transfer between Sb₂Se₃ and FTO. Thermally evaporated devices deposited on CdS do not show the same evidence of intermixing between the Sb₂Se₃ and CdS layers from EQE measurements, shown in Fig. 4(d). Although CdS/Sb₂Se₃ intermixing has been previously reported [46], it has never been observed as a performance limiting factor. Indeed, work has been published showing CdS/Sb₂Se₃ devices with good efficiency using a CSS-like process.[47] However, the technique employed by Li *et al.* uses a rapid thermal deposition, without the extended high temperature exposure to allow intermixing as used in this work. To establish the degree of intermixing, TOF-SIMS analysis was performed on both evaporation and CSS deposited cells for comparison, with etching via cesium ions from the back face (i.e. Sb₂Se₃ side). Fig. 5(b) and 5(c) shows that in evaporated Sb₂Se₃ devices the Sb and Se contents evolve identically, yet these are offset in CSS devices; revealing a Se excess beyond the junction. The evaporated sample also shows overlaid Cd and S profiles, suggesting a well-defined CdS layer. In the CSS

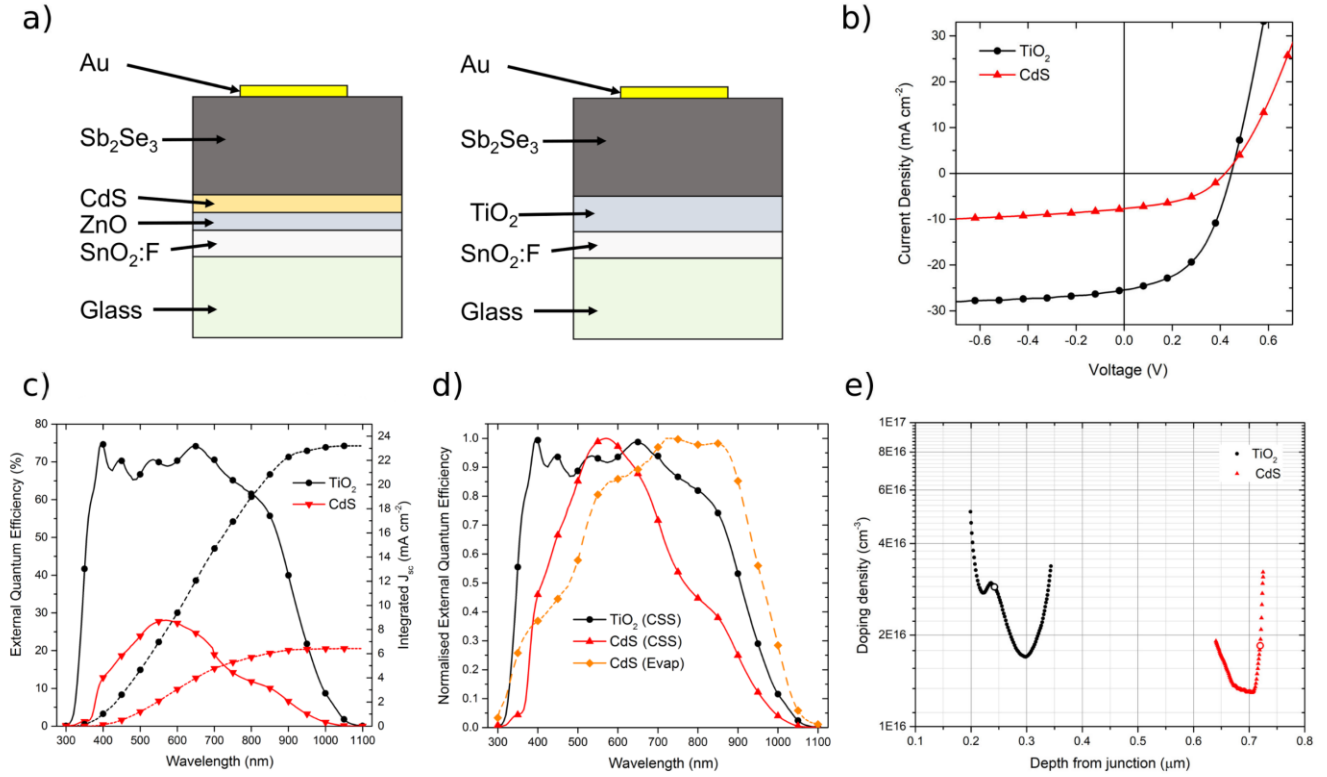


Fig. 4. CdS and TiO₂ window layer champion device architectures and electrical properties. a) Schematics showing the different window layers in each thin-film device, configured in the superstrate orientation. b) J-V curves of the devices. c) EQE spectra of the devices. Integrated J_{sc} for TiO₂ was 23.2 mA cm⁻², while the CdS was 6.42 mA cm⁻², showing a small difference compared to J_{sc} values extracted from J-V plots, which include a small amount of contact spreading. d) Normalized EQE spectra to highlight the regions of loss for the CSS devices. An evaporated device is included for comparison showing significantly fewer losses at wavelengths greater than 710 nm. e) Doping density depth profiles from C-V measurements, circle denotes 0V.

sample, Cd and S peaks are again offset: suggesting excess Cd towards the back-surface relative to the S. From these profiles, we can infer the presence of a detrimental CdSe interlayer in the CSS device that is absent in the evaporated sample. Again, we may draw commonalities with CdTe work, as it has been established that the degree of CdS intermixing for thermally evaporated deposition is below that of CSS deposited films. Sulfur has been shown to move via a grain-boundary assisted process that is enhanced by higher temperatures whereby the grain-boundary width is large compared to the diffusion coefficient in a Type-C mechanism [9], [45], [48]. This enhanced diffusion demonstrates the fundamental change for CSS deposition of Sb₂Se₃ and shows that, unlike for evaporated material, CdS is an unsuitable partner layer.

To mitigate the intermixing related issues and reduce parasitic absorption from the window layer, several metal oxides were considered to replace the CdS due to their typically wide bandgaps and high stability. Zinc oxide and tin oxide were two obvious choices, given the previous success observed in the literature [4], [49], and compatibility with FTO. However, unlike other deposition routes, both these materials yielded very low device efficiencies of <1% and therefore were abandoned in favor of TiO₂, a common and well characterized electron extraction layer frequently utilized in dye-sensitized and hybrid perovskite solar cells, as in Fig. 5(a,ii) [50]. There was also prior work on TiO₂ using solution processed Sb₂Se₃, which although giving an efficiency of only 2.26%, did produce a V_{oc}

TABLE II
DEVICE PARAMETERS FOR DIFFERENT WINDOW LAYERS

Window Layer	η (%)	V_{oc} (V)	J_{sc} (mA cm ⁻²)	FF (%)
CdS	1.44	0.42	7.57	45.48
	<i>0.74 ± 0.45</i>	<i>0.27 ± 0.09</i>	<i>7.18 ± 2.15</i>	<i>35.30 ± 5.64</i>
TiO ₂	5.48	0.45	25.44	48.96
	<i>4.68 ± 0.66</i>	<i>0.44 ± 0.01</i>	<i>24.83 ± 1.05</i>	<i>42.96 ± 4.65</i>

Peak (bold) and average ± standard deviation (italicized) cell performance parameters for the different cell structures with Sb₂Se₃ deposited by CSS. Average taken from the 9 contacts on each sample plate.

value over 0.5 V implying high suitability as a partner layer [8]. Other work on TiO₂ has been limited, but Chen *et al.* [23] have produced high efficiency devices on TiO₂. Using RTE, their V_{oc} of 0.358 V was significantly lower than CSS cells produced in this work, highlighting the importance of deposition method. Cells fabricated using a structure of FTO/TiO₂/Sb₂Se₃/Au, as in Fig. 4(b), were produced and found to generate consistently high performance of >4%. Following further optimization of the CSS deposition process to account for variations in growth between CdS and TiO₂ substrates, device quality layers were deposited. Fig. 4(c) shows J-V curves for the best devices from cells with CdS and TiO₂ partner layers, whilst associated EQE and C-V data is given in Fig. 4(d) and 4(e) respectively. The improvement in overall performance is clear from the J-V curves, with a marked improvement in series resistance and dramatically higher current values. The EQE spectra reveal no intermixing problems at longer wavelengths, while the higher

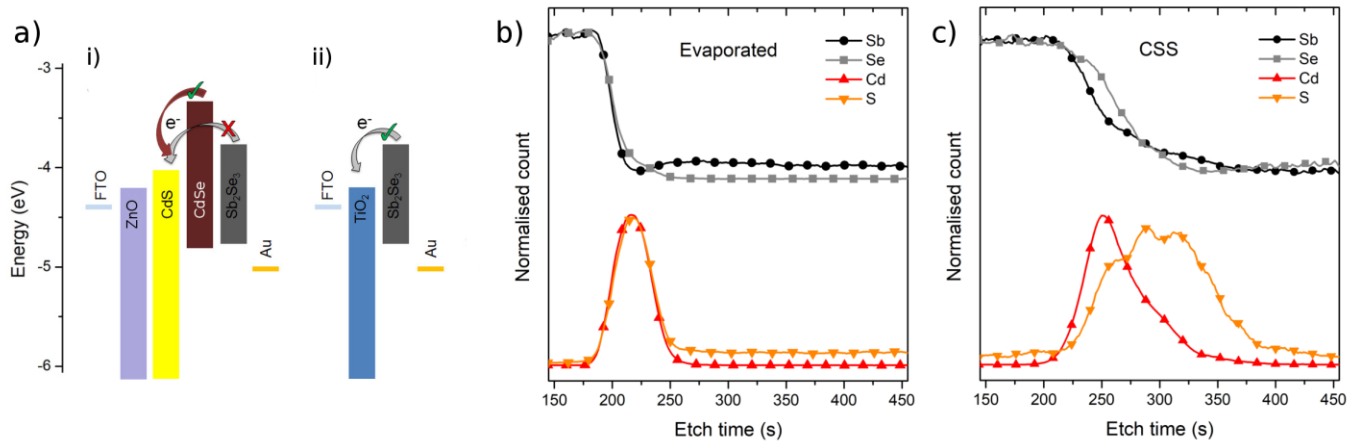


Fig. 5. CdS and TiO₂ window layer devices energy level schematic and SIMS profile providing evidence of electron extraction barrier. a.i) diagram of device with CdS window showing the barrier introduced by the formation of a CdSe interlayer which impedes charge extraction from the Sb₂Se₃ layer. a.ii) TiO₂ window layer, without the CdSe interlayer, with no extraction barrier b) normalized TOF-SIMS profiles showing overlaid traces for the evaporated material with no indication of an interlayer. Back surface = 0s c) normalized TOF-SIMS profiles showing the clear offset of Se relative to Sb and Cd relative to S in CSS deposited material at the Sb₂Se₃/CdS interface, indicating the presence of CdSe. Back surface = 0s

TiO₂ bandgap also leads to greatly improved short wavelength collection (<520 nm). V_{oc} values are improved on switching to TiO₂, typically in excess of 0.45 V, higher than some recent record devices [4], [14]. CSS produces material with a relatively high doping density of $>10^{16}\text{cm}^{-3}$, however, the TiO₂ sample shows only marginal improvement over CdS and the bulk of the enhancement is likely due to reduced interfacial recombination. The primary loss compared to current champion devices is due to a low FF value which we believe may be due to Se-rich phases at the surface which add additional resistance to the device, and from some shunting pathways which may be improved through additional modification of the CSS process to improve the coverage. Eliminating CdS from the device architecture has been shown to significantly improve device longevity [4], [23]. Improved device stability is a key factor in scaling up PV technologies, thus using alternative window layers, such as TiO₂, are a pivotal step in enabling a complete stack of scalable materials.

IV. CONCLUSIONS

This work demonstrates an industrially scalable close spaced sublimation (CSS) route to the fabrication of high efficiency Sb₂Se₃ solar cells with a particularly high V_{oc} . CSS films were shown to be markedly different to thermally evaporated material, with changes in grain structure, film orientation, optical properties and level of intermixing. The intermixing with the CdS n -type layer for CSS deposited films necessitated the re-design of the cell structure, owing to the formation of CdSe at the front interface. These devices had high V_{oc} values but were current limited and thus demonstrated lower performance. Several oxide alternatives were evaluated, such as ZnO and SnO₂, however replacing the CdS film with a TiO₂ partner layer led to a dramatic improvement in the J_{sc} while slightly improving the V_{oc} to 0.45 V, which exceeds the current champion device [14]. An efficiency of 5.48% was achieved, amongst the highest efficiency reported for TiO₂/Sb₂Se₃ devices, and there would appear to be a tremendous scope to improve on this given the nascent nature of the work. SLME

calculations predict an upper limit of 30% to be achievable for this technology and there are many fundamental questions which can be addressed to push the development of this technology. From our work and that of others, there are already three defined partner layers which have been demonstrated capable of producing devices of $>5\%$ PCE; namely CdS, ZnO, and TiO₂. As this work demonstrates, all layers are not suitable for all deposition routes and there are liable to be other, possibly more suitable, partner layers available. Our initial DFT calculations also suggest the likely presence of significant deep defect levels within the device structure such as V_{Se} . Development of effective post-growth treatment or passivation routines such as selenization or identifying an equivalent to the CdTe chloride treatment could limit the influence of these defects. The influence of extrinsic doping is also to be explored as is the concept of a substrate configuration device, which thus far has received negligible interest. Sb₂Se₃ is an emerging inorganic thin film technology of immense interest with the potential to develop rapidly by addressing these key challenges. There is a huge amount of scope to increase the performance of this technology by adopting knowledge and production process from other thin-film technologies, as this work demonstrates.

V. REFERENCES

- [1] T. D. Lee and A. U. Ebong, "A review of thin film solar cell technologies and challenges," *Renew. Sustain. Energy Rev.*, vol. 70, pp. 1286–1297, Apr. 2017, DOI: 10.1016/j.rser.2016.12.028.
- [2] M. L. Petrus *et al.*, "Capturing the Sun: A Review of the Challenges and Perspectives of Perovskite Solar Cells," *Adv. Energy Mater.*, vol. 7, no. 16, p. 1700264, Aug. 2017, DOI: 10.1002/aenm.201700264.
- [3] Y. Zhou *et al.*, "Thin-film Sb₂Se₃ photovoltaics with oriented one-dimensional ribbons and benign grain boundaries," *Nat. Photonics*, vol. 9, no. 6, pp. 409–415, 2015, DOI: 10.1038/nphoton.2015.78.
- [4] L. Wang *et al.*, "Stable 6%-efficient Sb₂Se₃ solar cells with a ZnO buffer layer," *Nat. Energy*, vol. 2, no. 4, p. 17046, Mar. 2017, DOI: 10.1038/nenergy.2017.46.
- [5] G. P. Voutsas, A. G. Papazoglou, P. J. Rentzeperis, and D. Siapkas, "The crystal structure of antimony selenide, Sb₂Se₃," *Zeitschrift für Krist. - New Cryst. Struct.*, vol. 171, no. 3–4, pp. 261–268, 1985, DOI: 10.1524/zkri.1985.171.3-4.261.

- [6] M. Birkett *et al.*, “Band gap temperature-dependence of close-space sublimation grown Sb_2Se_3 by photo-reflectance,” *APL Mater.*, vol. 6, no. 8, p. 084901, Aug. 2018, DOI: 10.1063/1.5027157.
- [7] N. W. Tideswell, F. H. Kruse, and J. D. McCullough, “The crystal structure of antimony selenide, Sb_2Se_3 ,” *Acta Crystallogr.*, vol. 10, no. 2, pp. 99–102, Feb. 1957, DOI: 10.1107/S0365110X57000298.
- [8] Y. Zhou *et al.*, “Solution-Processed Antimony Selenide Heterojunction Solar Cells,” *Adv. Energy Mater.*, vol. 4, no. 8, p. 1301846, Jun. 2014, DOI: 10.1002/aenm.201301846.
- [9] J. D. Major, “Grain boundaries in CdTe thin film solar cells: a review,” *Semicond. Sci. Technol.*, vol. 31, no. 9, p. 093001, Sep. 2016, DOI: 10.1088/0268-1242/31/9/093001.
- [10] R. E. Brandt, V. Stevanović, D. S. Ginley, and T. Buonassisi, “Identifying defect-tolerant semiconductors with high minority-carrier lifetimes: beyond hybrid lead halide perovskites,” *MRS Commun.*, vol. 5, no. 02, pp. 265–275, Jun. 2015, DOI: 10.1557/mrc.2015.26.
- [11] A. M. Ganose, C. N. Savory, and D. O. Scanlon, “Beyond methylammonium lead iodide: prospects for the emergent field of ns2 containing solar absorbers,” *Chem. Commun.*, vol. 53, no. 1, pp. 20–44, 2017, DOI: 10.1039/C6CC06475B.
- [12] Y. C. Choi *et al.*, “ Sb_2Se_3 -Sensitized Inorganic-Organic Heterojunction Solar Cells Fabricated Using a Single-Source Precursor,” *Angew. Chemie Int. Ed.*, vol. 53, no. 5, pp. 1329–1333, Jan. 2014, DOI: 10.1002/anie.201308331.
- [13] K. Zeng, D.-J. Xue, and J. Tang, “Antimony selenide thin-film solar cells,” *Semicond. Sci. Technol.*, vol. 31, no. 6, p. 063001, 2016, DOI: 10.1088/0268-1242/31/6/063001.
- [14] X. Wen *et al.*, “Vapor transport deposition of antimony selenide thin film solar cells with 7.6% efficiency,” *Nat. Commun.*, vol. 9, no. 1, p. 2179, Dec. 2018, DOI: 10.1038/s41467-018-04634-6.
- [15] M. Luo *et al.*, “Thermal evaporation and characterization of superstrate CdS/ Sb_2Se_3 solar cells,” vol. 173904, no. 2014, 2015, DOI: 10.1063/1.4874878.
- [16] C. Yuan, X. Jin, G. Jiang, W. Liu, and C. Zhu, “ Sb_2Se_3 solar cells prepared with selenized dc-sputtered metallic precursors,” *J. Mater. Sci. Mater. Electron.*, vol. 27, no. 9, pp. 8906–8910, Sep. 2016, DOI: 10.1007/s10854-016-4917-3.
- [17] T. T. Ngo, S. Chavhan, I. Kosta, O. Miguel, H.-J. Grande, and R. Tena-Zaera, “Electrodeposition of Antimony Selenide Thin Films and Application in Semiconductor Sensitized Solar Cells,” *ACS Appl. Mater. Interfaces*, vol. 6, no. 4, pp. 2836–2841, Feb. 2014, DOI: 10.1021/am405416a.
- [18] L. J. Phillips *et al.*, “Close-Spaced Sublimation for Sb_2Se_3 Solar Cells,” in *IEEE 44th Photovoltaic Specialist Conference (PVSC)*, 2017.
- [19] G. Li *et al.*, “Self-powered, high-speed Sb_2Se_3 /Si heterojunction photodetector with close spaced sublimation processed Sb_2Se_3 layer,” *J. Alloys Compd.*, vol. 737, pp. 67–73, Mar. 2018, DOI: 10.1016/j.jallcom.2017.12.039.
- [20] O. S. Hutter, L. J. Phillips, K. Durose, and J. D. Major, “6.6% efficient antimony selenide solar cells using grain structure control and an organic contact layer,” *Sol. Energy Mater. Sol. Cells*, vol. 188, pp. 177–181, Dec. 2018, DOI: 10.1016/j.solmat.2018.09.004.
- [21] Z. Li *et al.*, “ Sb_2Se_3 thin film solar cells in substrate configuration and the back contact selenization,” *Sol. Energy Mater. Sol. Cells*, vol. 161, no. November 2016, pp. 190–196, Mar. 2017, DOI: 10.1016/j.solmat.2016.11.033.
- [22] C. Yuan, L. Zhang, W. Liu, and C. Zhu, “Rapid thermal process to fabricate Sb_2Se_3 thin film for solar cell application,” *Sol. Energy*, vol. 137, pp. 256–260, 2016, DOI: 10.1016/j.solener.2016.08.020.
- [23] C. Chen *et al.*, “Accelerated Optimization of TiO_2 / Sb_2Se_3 Thin Film Solar Cells by High-Throughput Combinatorial Approach,” *Adv. Energy Mater.*, vol. 7, no. 20, p. 1700866, Oct. 2017, DOI: 10.1002/aenm.201700866.
- [24] J. Major, “CdTe solar cells : growth phenomena and device performance,” University of Durham, 2008.
- [25] C. Ferekides *et al.*, “High efficiency CSS CdTe solar cells,” *Thin Solid Films*, vol. 361–362, pp. 520–526, 2000, DOI: [http://dx.doi.org/10.1016/S0040-6090\(99\)00824-X](http://dx.doi.org/10.1016/S0040-6090(99)00824-X).
- [26] D. H. Rose, D. H. Levi, R. J. Matson, D. S. Albin, R. G. Dhere, and P. Sheldon, “The role of oxygen in CdS/CdTe solar cells deposited by close-spaced sublimation,” in *Conference Record of the Twenty Fifth IEEE Photovoltaic Specialists Conference - 1996*, 1996, pp. 777–780, DOI: 10.1109/PVSC.1996.564243.
- [27] C. Chen *et al.*, “6.5% Certified Efficiency Sb_2Se_3 Solar Cells Using PbS Colloidal Quantum Dot Film as Hole-Transporting Layer,” *ACS Energy Lett.*, vol. 2, no. 9, pp. 2125–2132, Sep. 2017, DOI: 10.1021/acsenergylett.7b00648.
- [28] G. Kresse and J. Hafner, “Ab initio molecular dynamics for liquid metals,” *Phys. Rev. B*, vol. 47, no. 1, pp. 558–561, Jan. 1993, DOI: 10.1103/PhysRevB.47.558.
- [29] G. Kresse and J. Hafner, “Ab initio molecular-dynamics simulation of the liquid-metal amorphous-semiconductor transition in germanium,” *Phys. Rev. B*, vol. 49, no. 20, pp. 14251–14269, 1994, DOI: 10.1103/PhysRevB.49.14251.
- [30] G. Kresse and J. Furthmüller, “Efficient iterative schemes for ab initio total-energy calculations using a plane-wave basis set,” *Phys. Rev. B*, vol. 54, no. 16, pp. 11169–11186, 1996, DOI: 10.1103/PhysRevB.54.11169.
- [31] G. Kresse and J. Furthmüller, “Efficiency of ab-initio total energy calculations for metals and semiconductors using a plane-wave basis set,” *Comput. Mater. Sci.*, vol. 6, no. 1, pp. 15–50, Jul. 1996, DOI: 10.1016/0927-0256(96)00008-0.
- [32] A. V. Kruckau, O. A. Vydrov, A. F. Izmaylov, and G. E. Scuseria, “Influence of the exchange screening parameter on the performance of screened hybrid functionals,” *J. Chem. Phys.*, vol. 125, no. 22, p. 224106, 2006, DOI: <http://dx.doi.org/10.1063/1.2404663>.
- [33] S. Grimme, “Accurate description of van der Waals complexes by density functional theory including empirical corrections,” *J. Comput. Chem.*, vol. 25, pp. 1463–1473, 2004, DOI: 10.1002/jcc.20078.
- [34] J. P. Perdew, K. Burke, and M. Ernzerhof, “Generalized Gradient Approximation Made Simple,” *Phys. Rev. Lett.*, vol. 77, no. 18, pp. 3865–3868, Oct. 1996, DOI: 10.1103/PhysRevLett.77.3865.
- [35] P. E. Blöchl, “Projector augmented-wave method,” *Phys. Rev. B*, vol. 50, no. 24, pp. 17953–17979, Dec. 1994, DOI: 10.1103/PhysRevB.50.17953.
- [36] M. Gajdoš, K. Hummer, G. Kresse, J. Furthmüller, and F. Bechstedt, “Linear optical properties in the projector-augmented wave methodology,” *Phys. Rev. B*, vol. 73, no. 4, p. 45112, Jan. 2006, DOI: 10.1103/PhysRevB.73.045112.
- [37] L. Yu and A. Zunger, “Identification of Potential Photovoltaic Absorbers Based on First-Principles Spectroscopic Screening of Materials,” *Phys. Rev. Lett.*, vol. 108, no. 6, p. 68701, Feb. 2012, DOI: 10.1103/PhysRevLett.108.068701.
- [38] M. R. Filip, C. E. Patrick, and F. Giustino, “GW quasiparticle band structures of stibnite, antimonselite, bismuthinite, and guanajuatite,” *Phys. Rev. B*, vol. 87, no. 20, p. 205125, May 2013, DOI: 10.1103/PhysRevB.87.205125.
- [39] W. Siemons *et al.*, “Dielectric-Constant-Enhanced Hall Mobility in Complex Oxides,” *Adv. Mater.*, vol. 24, no. 29, pp. 3965–3969, 2012, DOI: 10.1002/adma.201104665.
- [40] P. Schmidt, M. Binnewies, R. Glaum, and M. Schmidt, “Chemical Vapor Transport Reactions—Methods, Materials, Modeling,” in *Advanced Topics on Crystal Growth*, InTech, 2013, DOI: 10.5772/55547.
- [41] J. D. Major, Y. Y. Proskuryakov, K. Durose, G. Zoppi, and I. Forbes, “Control of grain size in sublimation-grown CdTe, and the improvement in performance of devices with systematically increased grain size,” *Sol. Energy Mater. Sol. Cells*, vol. 94, no. 6, pp. 1107–1112, Jun. 2010, DOI: 10.1016/j.solmat.2010.02.034.
- [42] J. Luschnitz, K. Lakus-Wollny, A. Klein, and W. Jaegermann, “Growth regimes of CdTe deposited by close-spaced sublimation for application in thin film solar cells,” *Thin Solid Films*, vol. 515, no. 15, pp. 5814–5818, May 2007, DOI: 10.1016/j.tsf.2006.12.171.
- [43] T. Hahn, Ed., *International Tables for Crystallography*, vol. A. Chester, England: International Union of Crystallography, 2006, DOI: 10.1107/97809553602060000100.
- [44] J. M. Kephart, R. M. Geisthardt, Z. Ma, J. McCamy, and W. S. Sampath, “Reduction of window layer optical losses in CdS/CdTe solar cells using a float-line manufacturable HRT layer,” in *2013 IEEE 39th Photovoltaic Specialists Conference (PVSC)*, 2013, pp. 1653–1657, DOI: 10.1109/PVSC.2013.6744462.
- [45] A. A. Taylor *et al.*, “A comparative study of microstructural stability and sulphur diffusion in CdS/CdTe photovoltaic devices,” *Sol. Energy Mater. Sol. Cells*, vol. 141, pp. 341–349, Oct. 2015, DOI: 10.1016/j.solmat.2015.06.010.
- [46] Y. Zhou *et al.*, “Buried homojunction in CdS/ Sb_2Se_3 thin film photovoltaics generated by interfacial diffusion,” *Appl. Phys. Lett.*,

- vol. 111, no. 1, p. 013901, Jul. 2017, DOI: 10.1063/1.4991539.
- [47] D.-B. Li *et al.*, “Stable and efficient CdS/Sb₂Se₃ solar cells prepared by scalable close space sublimation,” *Nano Energy*, vol. 49, pp. 346–353, Jul. 2018, DOI: 10.1016/j.nanoen.2018.04.044.
- [48] A. F. W. Willoughby, “Narrow-gap II-VI Compounds for Optoelectronic and Electromagnetic Applications,” in *Narrow-gap II-VI Compounds for Optoelectronic and Electromagnetic Applications*, P. Capper, Ed. Springer US, 1997, pp. 268–289.
- [49] S. Lu *et al.*, “Sb₂Se₃ Thin-Film Photovoltaics Using Aqueous Solution Sprayed SnO₂ as the Buffer Layer,” *Adv. Electron. Mater.*, p. 1700329, Dec. 2017.
- [50] S. Mariotti, O. S. Hutter, L. J. Phillips, P. J. Yates, B. Kundu, and K. Durose, “Stability and Performance of CsPbI₃Br Thin Films and Solar Cell Devices,” *ACS Appl. Mater. Interfaces*, vol. 10, no. 4, pp. 3750–3760, Jan. 2018, DOI: 10.1021/acsami.7b14039.
- [51] C. J. Bradley and A. P. Cracknell, *Mathematical Theory of Symmetry in Solids*. Oxford University Press, 1972.